Accelerated Short Circuiting in Anode-Free Solid-State Batteries Driven by Local Lithium Depletion

*John A. Lewis[1], Stephanie Elizabeth Sandoval[1], Yuhgene Liu[1], Douglas Lars Nelson[1], Sun Geun Yoon[2], Mengkun Tian[3], Pavel Shevchenko[4], Matthew T. McDowell[1,2]**

[1]School of Materials Science and Engineering, Georgia Institute of Technology, 771 Ferst Drive, Atlanta, GA, 30332
[2]George W. Woodruff School of Mechanical Engineering, Georgia Institute of Technology, 801 Ferst Drive, Atlanta, GA, 30332
[3]Institute for Electronics and Nanotechnology, Georgia Institute of Technology, Atlanta, GA, 30332, USA
[4]Advanced Photon Source, Argonne National Laboratory, Lemont, IL, USA

*Corresponding Author: mattmcdowell@gatech.edu

Abstract

"Anode-free" solid-state batteries (SSBs), which have no active material at the anode and undergo *in situ* lithium plating during the first charge, can exhibit extremely high energy density (~1500 Wh L^{-1}). However, there is a lack of understanding of lithium plating/stripping mechanisms at bare solid-state electrolyte (SSE) interfaces since excess lithium is often used. Here, we demonstrate that commercially relevant quantities of lithium (> 5 mAh cm^{-2}) can be reliably plated at relatively high current densities (1 mA cm^{-2}) using the sulfide SSE Li_6PS_5Cl. Investigations of lithium plating/stripping mechanisms, in conjunction with cryo-focused ion beam (FIB) and *ex situ* synchrotron tomography, reveal that the cycling stability of these cells is intrinsically limited by spatially uneven plating/stripping. Local lithium depletion toward the end of stripping decreases electrochemically active area, which results in high local current densities and void formation, accelerating subsequent filament growth and short circuiting compared to lithium-excess cells. Despite this governing degradation mode, we show that anode-free cells exhibit comparable Coulombic efficiencies to lithium-excess cells before short circuiting, and improved resistance to short-circuiting is achieved by avoiding local lithium depletion through retention of lithium at the interface. These new insights provide a foundation for engineering future high-energy anode-free SSBs.

1. Introduction

Solid-state batteries (SSBs) could provide higher energy density than conventional lithium-ion batteries by enabling the use of the lithium metal anode[1–5]. Lithium metal SSBs with "anode-free" architectures have recently attracted attention due to the advantages of eliminating excess lithium metal (Fig. 1a)[6,7]. In an anode-free (or zero-lithium-excess) SSB, the cell is initially assembled without active material at the anode, and the anode is formed *in situ* by plating lithium pre-stored in the cathode[6–11]. Key advantages are the reduction in cell stack volume by ~15%, resulting in a large increase in energy density (Fig. 1a), as well as the removal of the need to handle air-sensitive lithium metal in a manufacturing environment[7,11]. Anode-free SSB architectures could therefore increase energy density while also simplifying manufacturing and lowering cell costs.

While there is great interest in anode-free SSBs[6,7], achieving stable cycling in these cells is challenging[12,13]. One reason is that it is difficult to create uniform physical contact (i.e., without voids) between the solid-state electrolyte (SSE) and metal current collectors to enable initial lithium plating at high current densities, in contrast to soft lithium metal which can deform to contact the SSE. Poor interfacial contact will increase the local current density in some regions[14–17], promoting the growth of lithium filaments that can short circuit the cell[18–22]. Additionally, the Coulombic efficiency (CE) of anode-free cells must be very high since there is no excess lithium to compensate for lithium loss due to side reactions. Lithium metal anodes in both SSBs and liquid electrolytes have been observed to exhibit relatively low CEs[23,24], making this challenge difficult to solve. Designing viable anode-free SSBs therefore requires a detailed understanding of contact evolution, lithium filament growth, and capacity retention during plating and stripping at current collector/SSE interfaces.

Despite growing interest, there has been relatively little work studying the mechanisms of plating and stripping in anode-free SSBs. Some studies have plated and stripped lithium on current collectors to measure Coulombic efficiency[25–27], but they did not investigate the underlying mechanisms at these interfaces. Anode-free cells have also been used to observe lithium electrodeposition[28–32], but these configurations were generally chosen to avoid the challenges of probing buried interfaces. Recently, Wang et. al demonstrated that ≥ 3 mAh cm^{-2} of Li could be cycled at interfaces between current collectors and the garnet $Li_7La_3Zr_2O_{12}$ (LLZO) SSE[12]. However, these cells operated at relatively low current densities (≤ 0.3 mA cm^{-2}) and required hot pressing current collectors onto LLZO at temperatures > 900 °C for fabrication. Other work has investigated anode-free SSBs using the softer Li_6PS_5Cl (LPSC) SSE[13], finding that performance

was limited by the poor deposition morphology of lithium at intrinsic current collector interfaces. This led to the incorporation of a Ag-C layer between the current collector and SSE, which facilitated uniform deposition. Although these cells exhibited excellent performance[13], the relatively thick mediator layers reduce energy density. Despite these advances, much is still unknown about how the plating and stripping mechanisms at interfaces with zero initial lithium metal differ from interfaces with excess lithium metal, which are much more commonly studied.

Here, we investigate the mechanisms of plating and stripping lithium metal within anode-free full and half cells using the sulfide Li_6PS_5Cl as the SSE. Simple cold pressing of copper foil onto LPSC at 15 MPa and room temperature enables the deposition of large amounts of compact lithium metal (> 5 mAh cm^{-2}) at a relatively high current density of 1 mA cm^{-2} during the initial *in situ* plating step. Despite impressive plating performance, we show that anode-free cells are fundamentally more prone to short circuiting than lithium-excess cells. This intrinsic propensity for short circuiting arises because nonuniform stripping and/or plating leads to localized lithium depletion and loss of electrochemically active area toward the end of the stripping step, and oxidation at these remaining lithium regions causes current focusing and void formation. Subsequent plating induces premature short circuiting compared to lithium-excess cells due to the exacerbated growth of lithium filaments at current constrictions. Interestingly, anode-free full cells were found to exhibit comparable CEs to lithium-excess full cells, suggesting that the capacity retention of anode-free SSBs during cycling would be similar to cells with excess lithium if short circuiting can be prevented. These findings show that filament growth and short circuiting due to the nonuniform removal of the last lithium from the interface is the key limiting factor for anode-free sulfide SSBs, and strategies to mitigate this degradation mode could enable high-performance anode-free SSBs. To this end, we investigated how preventing localized lithium depletion by retaining a lithium film at the interface can greatly improve the cycling stability of anode-free SSB cells.

2. Results and Discussion

2.1 Lithium deposition behavior at anode-free interfaces

We first studied the initial electrodeposition behavior of lithium metal in anode-free Cu/LPSC/Li half cells. In these half cells, a 10 μm copper foil current collector was cold pressed onto one side of a dense LPSC layer at ~15 MPa of stack pressure. A thick lithium metal foil (~0.3 mm) was simultaneously pressed onto the other side of the LPSC to serve as the lithium source.

Figure 1b shows a typical voltage profile when depositing lithium metal onto copper foil at 1 mA cm^{-2}. A nucleation overpotential associated with the initial formation of the lithium metal layer was observed at the beginning of deposition, and the voltage then stabilized to -50 mV. Notably, this cell (Fig. 1b) was able to plate over 6.5 mAh cm^{-2} before a short circuit occurred, as indicated by the sudden step in the voltage. Electrochemical impedance spectroscopy (EIS) measurements recorded throughout the deposition showed that the assembled cell initially had a very large impedance, which rapidly decreased to a total impedance of ~45 Ω cm^2 after nucleating lithium metal before transitioning into different stages of short circuiting (Fig. S1).

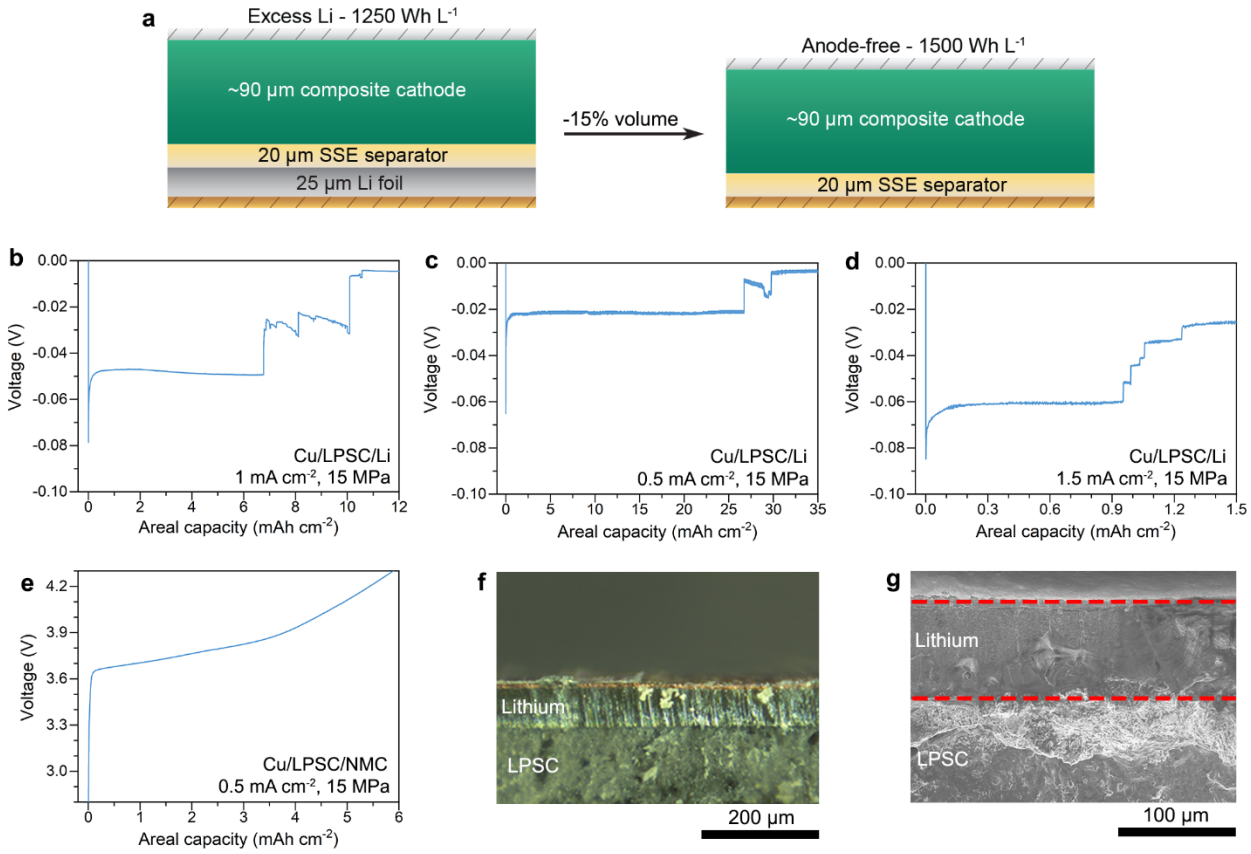

Figure 1. a) Transitioning from using an excess lithium foil as the anode (left) to an anode-free configuration (right) would reduce the stack volume by ~15% and increase energy density. **b)** Depositing lithium metal onto copper foil at 1 mA cm^{-2} in an anode free Cu/LPSC/Li half cell with a stack pressure of 15 MPa. **c)** Depositing lithium metal onto copper foil at 0.5 mA cm^{-2} and 15 MPa. **d)** Depositing lithium metal onto copper foil at 1.5 mA cm^{-2} and 15 MPa. **e)** Charging an anode-free Cu/LPSC/NMC full cell with a cathode loading of 6 mAh cm^{-2} at 0.5 mA cm^{-2} and 15 MPa. **f, g)** Optical and SEM images of thick lithium layers deposited at 0.5 mA cm^{-2} in half cells.

Additional experiments were conducted to understand how lithium deposition is impacted by different cell conditions. Figures 1c, d show the voltage profiles for deposition at current densities of 0.5 mA cm^{-2} and 1.5 mA cm^{-2}, respectively. Over 25 mAh cm^{-2} (125+ μm of lithium) was plated at 0.5 mA cm^{-2}, whereas only 1 mAh cm^{-2} was possible at 1.5 mA cm^{-2} before short circuiting. This behavior is similar to symmetric cells with thick lithium foil electrodes, where the current density plays a key role in how much lithium capacity can be passed before a short circuit forms[21]. Figure 1e shows that *in situ* lithium deposition was also possible in anode-free full cells where the lithium was initially stored in the $LiNi_{0.6}Mn_{0.2}Co_{0.2}O_2$ (NMC) composite cathode. In this cell, nearly all of the 6 mAh cm^{-2} cathode loading was utilized when charging at 0.5 mA cm^{-2}, demonstrating that large amounts of lithium could be accessed even with thick cathodes.

Stack pressure was found to impact anode-free deposition behavior (Fig. S2). Plating at a current density of 1 mA cm^{-2} and a lower stack pressure of 6 MPa yielded slightly less capacity before shorting compared to Fig. 1b. This cell also exhibited greater voltage polarization, suggesting that voids could be forming at the stripping interface due to lower rates of lithium deformation. Interestingly, the higher stack pressure of 40 MPa resulted in even lower deposited lithium capacities before short circuiting, despite larger stack pressures typically enhancing interfacial contact. We speculate that this could be due to deformation of the deposited lithium into porosity within the SSE, creating regions with higher effective current densities[21,33]. These findings indicate that future studies are needed to thoroughly assess the effects of stack pressure on anode-free deposition behavior.

Optical microscopy and scanning electron microscopy (SEM) were used to image cross-sections of samples that had thick lithium layers deposited *in situ* at 0.5 mA cm^{-2} (Figs. 1f, g). The optical image in Fig. 1f shows a layer with a lustrous silver appearance that is typical for pristine lithium metal, and the SEM image in Fig. 1g shows a thick layer of lithium on LPSC. Energy dispersive X-ray spectroscopy (EDS) maps taken of a different SEM cross-section only showed an abundance of oxygen in the deposited layer (Fig. S3), consistent with the elemental signature of lithium metal that has been briefly oxidized during sample transfer. X-ray photoelectron spectroscopy (XPS) experiments were also conducted on the deposited layer to confirm that the material was lithium metal (Fig. S4). The Li 1s and O 1s spectra showed the presence of Li_2O and Li_2O_2 species[34], which could be explained by the surface contamination layer on lithium metal. The absence of peaks in the Cl 2p and P 2p spectra indicated that the Li 1s signal was not from the SSE[35], which was the only other possible source of lithium in this system. Although the S 2p spectrum exhibited a weak peak, this could possibly be explained by interactions between the

sample and H_2S in the glovebox. Given these combined characterization results, we conclude that the deposited layers are indeed lithium metal.

The ability to deposit > 5 mAh cm^{-2} of lithium at the relatively high current density of 1 mA cm^{-2} in half cells is remarkable given that the cell assembly only used uniaxial cold pressing at moderate stack pressures (15 MPa) to successfully interface copper foil with LPSC. This result contrasts with the challenges of interfacing an anode-free current collector with oxides, such as LLZO, which have required hot pressing at temperatures > 900 °C to form a viable interface[12]. This behavior is likely due to the lower yield strength of sulfides, especially compared to the hard and brittle nature of oxides like LLZO[36,37]. The ability of the SSE to locally deform to contact the current collector is thus an important factor in developing high-performance anode-free SSBs.

Cryogenic focused-ion beam (cryo-FIB) milling and SEM imaging were carried out to observe how the thickness and morphology of lithium varied at different locations across the interface after deposition. These experiments leveraged two important capabilities to provide detailed information about the deposition process. First, the anode-free architecture facilitated FIB milling through the entirety of the lithium deposit due to the thinness of the copper foil current collector (~10 μm). Second, milling at cryogenic temperatures was critical to prevent detrimental interactions of the lithium with the gallium beam and the LPSC. To highlight the advantages of cryogenic milling, two trenches were milled at different temperatures (-145 °C and 25 °C) next to each other on the same sample, as shown in Fig. S5. Major differences in lithium morphology were observed, with the region milled at room temperature exhibiting extensive porosity, beam damage, and lighter contrast, demonstrating the necessity of using cryo-FIB for reliably characterizing lithium in LPSC-based SSBs.

Figure 2 shows SEM images taken after cryo-FIB milling at different positions on three different electrode samples. The first sample (Fig. 2a, b) was extracted from a Cu/LPSC/Li half cell after depositing 3 mAh cm^{-2} of lithium (~15 μm) at a current density of 0.5 mA cm^{-2}. The two images show the Cu/Li/LPSC cross-section near the center (Fig. 2a) and edge (Fig. 2b) of the electrode. In each image, the top layer (brighter contrast) is the copper foil. Below that is the deposited lithium (darkest contrast) and then the LPSC electrolyte (intermediate contrast). SEM images from additional trenches on this sample are shown in Fig. S6. The lithium deposits in each image were ~15 μm thick regardless of the location on the sample, as expected based on the areal capacity that was plated. The lithium layer thus exhibited highly uniform thickness across the interface when plated at this current density (0.5 mA cm^{-2}). The smooth and continuous morphology of the lithium in Fig. 2a, b is similar to what was observed by Wang et al. at anode-

free interfaces using the LLZO SSE[12]. We note that these experiments only provide a handful of randomly-selected local snapshots of the lithium thickness, and that greater variation may not be captured here.

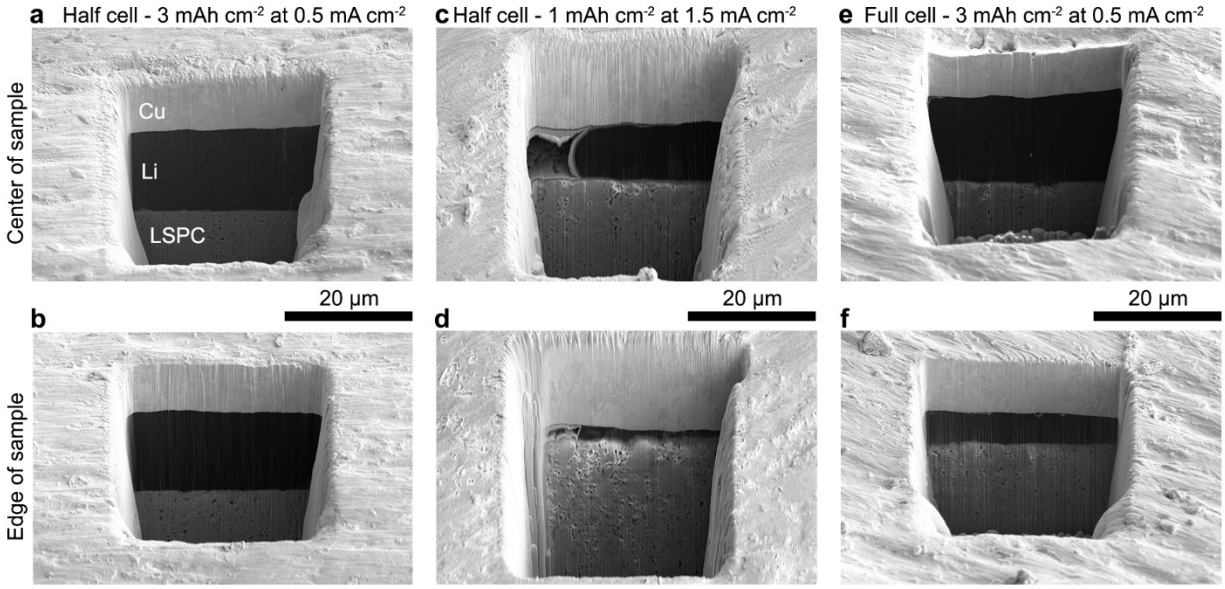

Figure 2. SEM images taken after cryo-FIB milling through anode-free Cu/LPSC interfaces after lithium deposition. Images in the top row were taken near the center of each electrode sample, while the images in the bottom row were taken near the edge of the electrode. **a, b)** 3 mAh cm^{-2} of lithium deposited at 0.5 mA cm^{-2} in a Cu/LPSC/Li half cell. **c, d)** 1 mAh cm^{-2} deposited at 1.5 mA cm^{-2} in a Cu/LPSC/Li half cell. **e, f)** 3 mAh cm^{-2} deposited at 0.5 mA cm^{-2} in a Cu/LPSC/NMC full cell.

The same cryo-FIB/SEM experiment was repeated for a half cell where 1 mAh cm^{-2} of lithium was deposited at the higher current density of 1.5 mA cm^{-2}. Two images from the center and edge are shown in Fig. 2c, d. The region at the center of the sample (Fig. 2c) had a lithium thickness of approximately 11 µm, exceeding the 5 µm that would be expected if deposition was ideally uniform. In contrast, a region at the edge of the electrode sample (Fig. 2d) had a lithium thickness of only 2 µm. Based on these results, it is apparent that higher current densities can cause the lithium to deposit with varying thickness across the electrode surface. This behavior could explain why much less capacity could be plated at 1.5 mA cm^{-2} before shorting compared to 0.5 mA cm^{-2} (Fig. 1c, d). The variation in lithium thickness across the interface suggests that regions with thicker lithium experienced higher local current densities, making it more likely that lithium filaments will form at these locations.

Deposition uniformity was also investigated for anode-free full cells. A Cu/LPSC/NMC full cell with a 3 mAh cm^{-2} cathode loading was charged with a current density of 0.5 mA cm^{-2} and subsequently characterized using cryo-FIB (Fig. 2e, f). An image of a trench cut in the center of the sample revealed a lithium thickness of 17 μm, while an image taken near the sample's edge showed a much smaller lithium thickness of 6 μm. Given these results, the full cell exhibited lower deposition uniformity compared to the half cell (Fig. 2a, b) despite using the same areal capacity and current density. However, both cells featured similar smooth and continuous lithium morphology. The reasons for these important differences in deposition uniformity are not entirely clear, and it is possible that different distribution of local stress due to the lack of a deformable lithium counter electrode in the full cell could play a role.

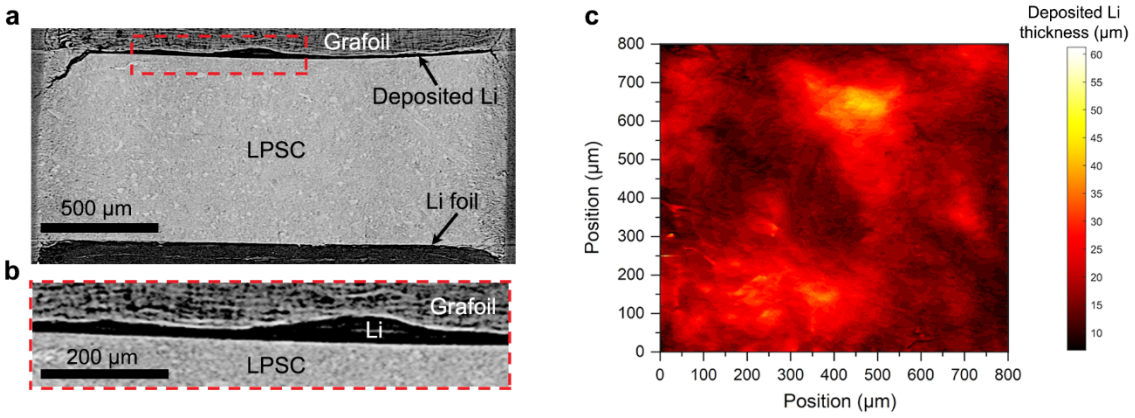

Figure 3. a) Reconstructed image slice taken from a synchrotron X-ray tomography scan of an anode-free half-cell after ~5.5 mAh cm^{-2} of lithium was deposited at 0.5 mA cm^{-2}. Grafoil was used as the deposition substrate due to the strong X-ray absorption of conventional current collectors like copper and steel, and the tomography cell featured a smaller diameter than cells used for other experiments herein. **b)** Magnified view of the deposited lithium showing variation of lithium thickness across the interface. **c)** Map of the deposited lithium thickness over an 800 μm by 800 μm area of the interface. Brighter colors represent regions with thicker lithium.

Cryo-FIB enables effective imaging of the deposited lithium metal, but this technique is limited by the relatively small size of the trenches milled (~30 μm by 30 μm in this study). To better understand the nature of lithium deposition across much larger interfacial regions, we leveraged synchrotron X-ray tomography to image an entire anode-free SSB after plating (see Methods for details). Figure 3a shows a reconstructed image slice collected from an X-ray tomography scan of an anode-free half cell after ~5.5 mAh cm^{-2} lithium was deposited at 0.5 mA cm^{-2}. Grafoil, a

commercial carbon-based conductive foil, was used as the deposition substrate due to the strong X-ray absorption of metal current collectors like copper and stainless steel that make it more difficult to discern the thin lithium layer at the interface. Although Grafoil is comprised of graphitic carbon that could possibly undergo Li intercalation, the galvanostatic electrochemical profile from this cell showed that negligible intercalation occurred, and the cell exhibited the typical nucleation overpotential and voltage plateau expected when depositing lithium (Fig. S7). Additionally, the deposited lithium layer was clearly detected at the Grafoil/LPSC interface in Fig. 3a-b.

The reconstructed image slices in Fig. 3a-b demonstrate that the thickness of the deposited lithium layer varies substantially. While the theoretical thickness value based on the amount of lithium deposited is ~25 μm, the magnified image of the interface (Fig. 3b) shows that the lithium thickness varies from approximately 40 μm at its thickest point to 14 μm in the thinnest region. This thickness variation was not attributed to variations in Grafoil morphology, since a pristine cell with a Grafoil current collector had a flat interface with the SSE before deposition (Fig. S8). Since the X-ray tomography scan generated 3D image data from the entire cell, we further analyzed thickness variation across a relatively large area of the interface. Figure 3c shows a two-dimensional map of the deposited lithium thickness as a function of position over an interfacial area of 800 μm by 800 μm at the center of the sample, with brighter colors representing regions with thicker lithium. The thickest lithium region is ~50 μm, while the thinnest is below 10 μm. Interestingly, the regions of greater thickness span hundreds of microns, indicating that higher current densities existed over relatively large areas. It is important to note that the X-ray tomography results should not be directly compared to the current density-dependent cryo-FIB data in Fig. 2, as the tomography experiments used smaller cell housings and smaller electrodes (see Methods), resulting in less uniform lithium thickness at the same current density. Overall, however, the results in Figs. 2-3 show that despite the ability to deposit relatively large amounts of lithium on bare current collectors, lithium can grow with nonuniform thickness at higher current densities. This finding is important because nonuniform lithium thickness can have consequences during stripping, as explored next.

2.2 Impact of stripping on cell reversibility

With an improved understanding of plating at anode-free LPSC interfaces, we next investigated how stripping impacts cell cycling. Figure 4a shows the typical behavior of an anode-free half cell cycled at 0.5 mA cm^{-2} with 3 mAh cm^{-2} capacity deposited per half cycle; this cell

short circuited in the third deposition cycle, and other identical cells showed similar rapid short circuiting. The cumulative lithium capacity plated at the Cu/LPSC interface in Fig. 4a was 6.5 mAh cm^{-2} (~32 μm total), which is far less than the 25 mAh cm^{-2} (~125 μm) achieved when plating continuously at the same current density (Fig. 1c), indicating that cyclic stripping severely diminishes performance and exacerbates short circuiting. The half cell in Fig. 4a exhibited a Coulombic efficiency of 90% on the first cycle, meaning that ~1.5 μm (0.3 mAh cm^{-2}) of lithium was left at the interface after the first stripping. It is notable that the stripping curves from the first and second cycles in Fig. 4a both show voltage increases near the end of stripping despite lithium being left at the interface. Such voltage polarization has been shown to be associated with the loss of electrochemically active area at the stripping interface[15–17].

Figure 4b shows typical cycling behavior of an anode-free full cell operated under the same conditions as the half cell in Fig. 4a. Interestingly, the full cell shorted in the ninth cycle instead of the third. The improved cyclability of the full cell over the half cell can partially be explained by the full cell's lower first-cycle CE (80%), indicating that a theoretical lithium thickness of ~2.5 μm (0.5 mAh cm^{-2}) remained at the anode current collector after the first discharge. The low initial CE in the full cell was primarily due to the cathode not reincorporating all the Li during discharge. Cryo-FIB characterization of an anode-free full cell after the first cycle showed that ~1.5 μm of lithium remained at the interface in the milled region (Fig. S9). The discrepancy between the ideal and actual amounts of lithium could be explained by deposition nonuniformity, as well as possible irreversible side reactions with the LPSC that can consume additional lithium. These results suggest that the slightly larger amount of lithium left at the interface after the first cycle in full cells can help improve cycling, although the beneficial effects of this extra lithium degrade over time since the cell still short circuits after the ninth cycle. A full cell using a thick lithium metal foil (~300 μm) as the anode was assembled and tested under the same conditions for comparison to the anode-free cells to better understand the mechanistic limitations of anode-free interfaces (Fig. 4c). Because the amount of lithium transferred per cycle was much lower than the thickness of the lithium foil, this cell always retained thick lithium metal at the anode/LPSC interface. This difference substantially enhanced cell performance, as the thick lithium foil full cell was able to complete over 100 cycles without short circuiting.

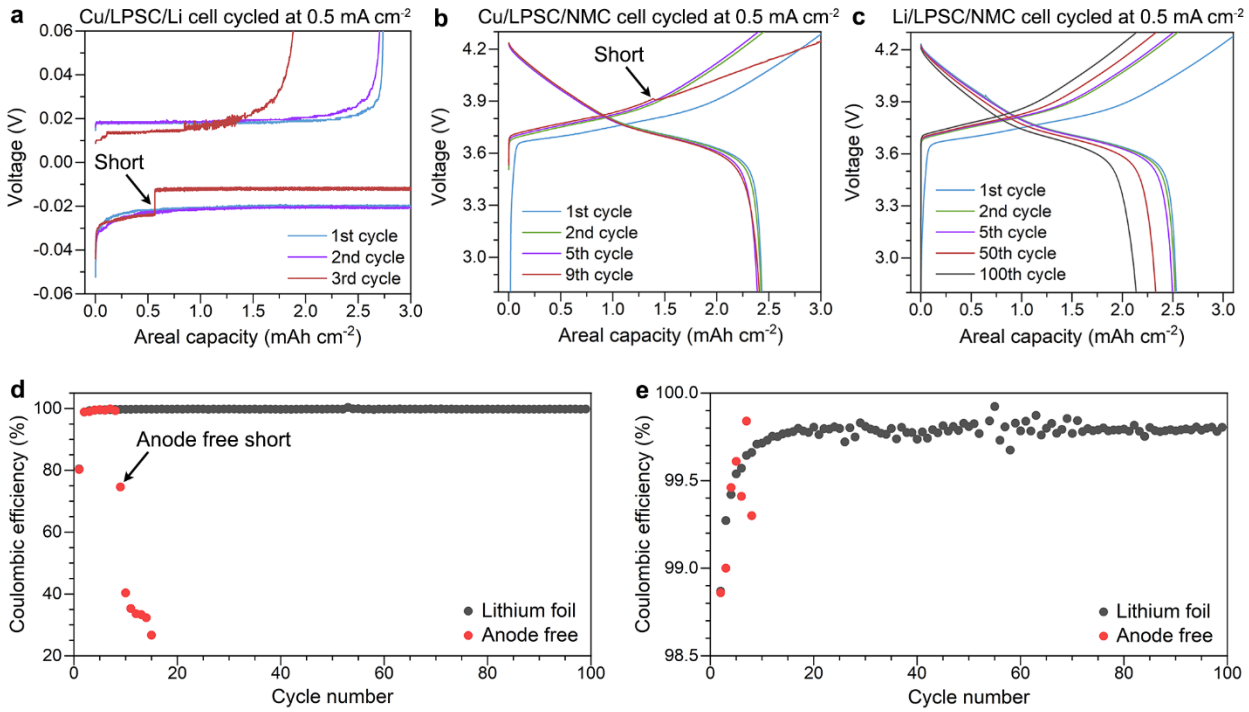

Figure 4. a) Cycling a Cu/LPSC/Li half cell at a current density of 0.5 mA cm^{-2} with a half-cycle capacity of 3 mAh cm^{-2}. **b)** Cycling a Cu/LPSC/NMC full cell at 0.5 mA cm^{-2} with a cathode loading of 3 mAh cm^{-2}. **c)** Cycling a lithium-excess Li/LPSC/NMC full cell at 0.5 mA cm^{-2} with a cathode loading of 3 mAh cm^{-2}. This cell used a lithium metal anode with a thickness of 0.3 mm. **d)** Comparison of the Coulombic efficiencies between the anode-free full cell (red circles) and the full cell with thick lithium foil (black circles). **e)** Magnified view of the plot in **(d)**.

These results have shown that anode-free cells are fundamentally limited by accelerated short circuiting compared to lithium-excess cells. Interestingly, however, we found that anode-free full cells using LPSC do exhibit high Coulombic efficiency and areal capacity (comparable to lithium-excess cells) before short circuiting. As shown in Fig. 4b-c, both types of cells were able to access the total cathode loading during the first charge, and both exhibited initial CEs of 80%. The CEs of subsequent cycles in the anode-free cell were also similar to the thick lithium foil cell (Fig. 4d, e), with the anode-free cell exhibiting an average CE of 99.3% during cycles 2-8 before shorting compared to 99.4% for the thick lithium foil. The lithium-excess full cell showed excellent performance beyond cycle 10 as well, with an average CE of 99.8%. The similar CEs of the two configurations show that the plating and stripping process in the anode-free SSBs are as efficient as in cells with excess lithium, which is surprising given that the lack of excess lithium in anode-free SSBs is generally thought to exacerbate lithium loss mechanisms. Our results instead

suggest that the critical limitation of anode-free SSBs is their greater propensity towards short circuiting.

Given these data, we now focus on why anode-free cells exhibit accelerated short circuiting. The underpinning mechanisms that differentiate anode-free SSBs from lithium-excess cells are schematically illustrated in Fig. 5a-d. In anode-free cells, lithium is initially deposited onto the current collector and can exhibit nonuniform thickness (Fig. 5a), suggesting that the current density can intrinsically vary across the interface. Near the end of the first stripping step (Fig. 5b), lithium is completely stripped from some regions of the anode, while some lithium regions remain. This behavior could be caused either by the initial nonuniform thickness of deposited lithium, slight variations of current collector morphology, or by natural variations of current density across the interface. Toward the end of stripping, there will therefore be some regions where lithium has been fully stripped and the SSE is in contact with the current collector ("inactive contact" in Fig. 5b), some regions of the SSE that have lost contact with the copper current collector ("physical gap" in Fig. 5b), and some regions were lithium remains in contact with the SSE.

We propose that the local depletion of lithium leading to isolated lithium contact regions (Fig. 5b) will play a dominant role in determining the cycling stability and propensity for short circuiting upon further cycling. This is because the formation of isolated lithium regions toward the end of stripping will decrease the electrochemically active area available for stripping, since the inactive Cu/SSE contacts and the physical gaps shown in Fig. 5b cannot support lithium oxidation. This decrease in electrochemically active interfacial area creates current constrictions at the remaining lithium regions, greatly increasing local current density. At some point during this process, the local stripping current density (j_{strip}) will exceed the critical current density for void formation (j_{void}) at some remaining lithium locations at the interface[15], and voids will form and accumulate at these lithium regions (Fig. 5c). Void formation will further decrease electrochemically active area and will also prevent these regions from being further stripped. This behavior can explain the inability to strip 100% of the deposited lithium in half cells, as demonstrated by the 90% Coulombic efficiency in Fig. 4a. After the stripping step, the current is reversed and plating begins at the interface (Fig. 5d). Lithium can be plated at all regions of metallic contact to the SSE, which likely cover a relatively large area of the interface. However, the isolated lithium regions at which voids formed at the end of stripping, as well as any physical gaps at the interface, will tend to cause current constrictions upon plating, which are well known to cause filament growth and short circuiting[15,17]. Some of the voids will be filled upon redeposition,

but it only takes a few regions of locally high current density ($j_{plate} > j_{filament}$) to cause filaments to form and grow.

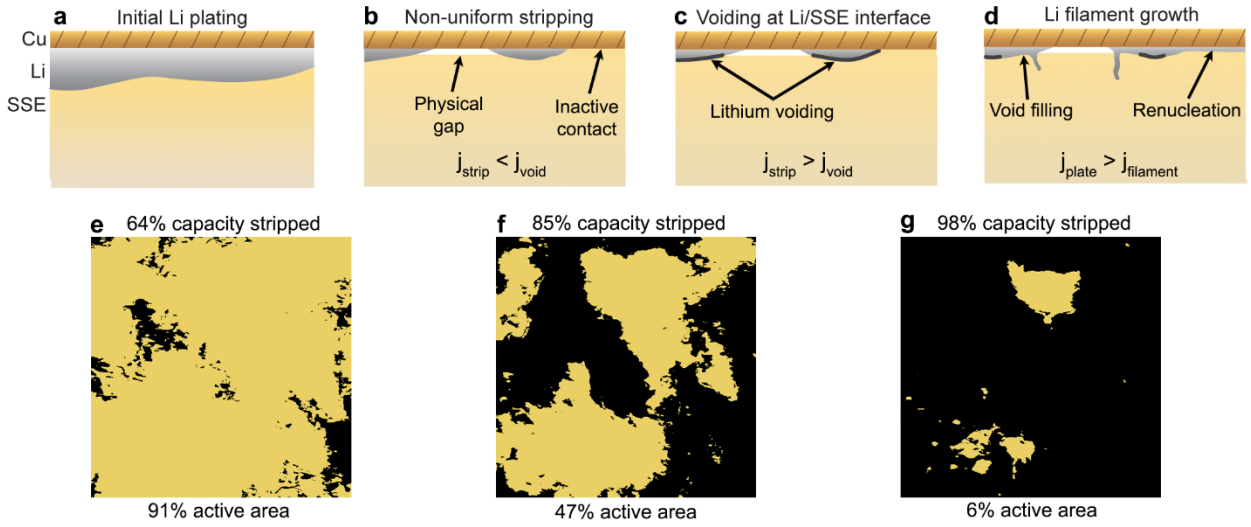

Figure 5. Schematic of plating and stripping mechanisms at anode-free interfaces. **a)** Lithium metal is initially deposited onto the current collector and can exhibit nonuniform thickness depending on current density. **b)** During early stripping, the effective current density (j_{strip}) is lower than the critical current density for void formation (j_{void}). After a large fraction of the capacity is stripped, some regions are completely depleted of Li and the electrochemically active area at the interface is reduced. **c)** Continuing to strip after losing active area results in a higher effective j_{strip} that exceeds j_{void} at some remaining lithium regions, leading to the formation of voids. **d)** When plating begins after stripping, current constrictions at the edges of previously-formed voids or gaps can cause local current densities j_{plate} to exceed the critical current density for filament growth, $j_{filament}$, leading to exacerbated filament growth at these locations. **e-g)** Simulated stripping using the synchrotron data in Fig. 3c by virtually removing one deposited lithium layer at a time. Black pixels represent regions where lithium has been fully depleted and is no longer present, reducing the electrochemically active area. The percentage of capacity stripped is labeled above each image, while the percentage of active area remaining is labeled below. The edge length of these images is 800 μm.

To support this proposed mechanism, we carried out further analysis of the *ex situ* synchrotron tomography data previously shown in Fig. 3. Based on the lithium thickness data across the interface in Fig. 3c, Fig. 5e-g shows snapshots of the electrochemically active contact area at the interface (i.e., regions of lithium contacting the LPSC) assuming that the lithium is stripped at a uniform rate from the interface. In this analysis, we simulated lithium stripping by removing lithium layer-by-layer. Due to the initial thickness variations, loss of electrochemically active area (i.e., lithium-SSE contact) occurs before 100% of the lithium capacity has been

stripped. Figure 5e shows that 91% of the area is active after stripping 64% of the lithium. Continuing to strip 85% of the total capacity dramatically decreases the active area to 47%, resulting in an actual current density 2.1 times the nominal value (Fig. 5f). In reality, this current density would be even higher in some regions due to current constriction effects. Reduction of electrochemically active area continues as more capacity is stripped, with isolated regions present at the end of stripping (Fig. 5g).

The plating/stripping mechanisms in anode-free SSBs are therefore fundamentally different from lithium-excess SSBs. The tendency for local lithium depletion and isolated lithium formation during stripping in anode-free SSBs is likely unavoidable at unaltered interfaces since neither deposition nor stripping will always occur with complete uniformity across the entire interface; the large lithium thickness variations observed in Fig. 3c are thus not necessary for this mechanism. Under these conditions, the local current density j_{strip} will increase locally and ultimately exceed j_{void} at remaining lithium regions due to the decrease in active area, even for relatively low applied current densities. This differs from lithium-excess SSBs, where there is never local depletion of lithium (i.e., lithium remains present across the entire interface) because of the thick lithium present. Voids can form during stripping in lithium-excess SSBs, but only when the global current density is greater than the critical current density for void formation, j_{void}. These concepts explain the improved resistance to short circuiting exhibited by lithium-excess cells (such as the full cell in Fig. 4c) compared to the anode-free full and half cells (Fig. 4a-b). The requirements for stable operation of anode-free SSBs are thus even more stringent than lithium-excess cells: in addition to preventing general physical contact loss and void formation, the key challenge for anode-free SSBs is to ensure that lithium is plated and stripped uniformly across the entire interface to minimize the localized depletion of lithium during stripping.

2.3. Controlling interfacial evolution to improve cyclability

The intrinsic local loss of electrochemically active area necessitates proper control over stripping behavior to maximize cell performance. To mitigate this degradation phenomenon, we explored the effects of initially depositing a relatively thick lithium layer and then cycling only a fraction of this layer. Our proposed degradation pathway suggests that this approach should mitigate short circuiting by avoiding local lithium depletion. Figure 6a shows an anode-free half cell operated at 0.5 mA cm^{-2}, where 3 mAh cm^{-2} was deposited initially and then cycled using only half of that capacity (1.5 mAh cm^{-2}). The stripping curves exhibit excellent stability without any voltage polarization over 75 cycles, indicating that the lithium layer was uniformly maintained

across the Cu substrate. In addition, no nucleation overpotentials were observed after the initial deposition, which is typical when depositing onto lithium metal[21] and is further evidence for lithium contact retention at the interface. The cell lifetime showed remarkable improvement compared to the case with full stripping (Fig. 4a), with a cumulative lithium capacity of ~114 mAh cm^{-2} being deposited onto Cu before a short circuit formed in the 75th cycle (red curve in Fig. 6a). A similar experiment (Fig. 6b) was conducted using an anode-free full cell with a cathode loading of 3 mAh cm^{-2}, with the cycling capacity controlled to be 1 mAh cm^{-2} after the first charge. This cell also showed improved cyclability compared to the full cell in Fig. 4b, lasting over 100 limited cycles without the formation of a short circuit.

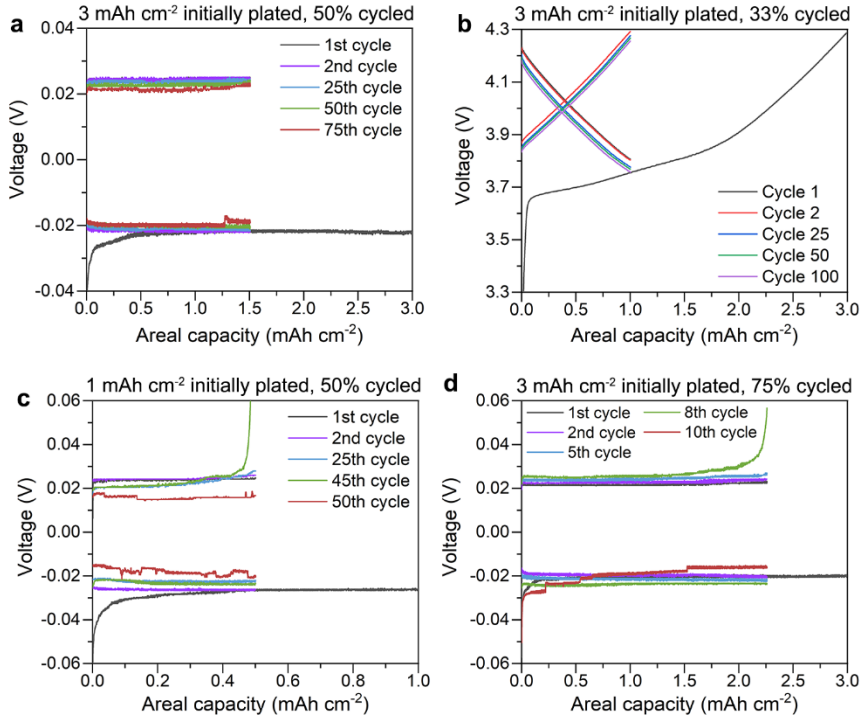

Figure 6. a) Capacity-limited cycling of a Cu/LPSC/Li half cell at 0.5 mA cm^{-2} with an initial deposition step of 3 mAh cm^{-2} and subsequent half cycles controlled to cycle 1.5 mAh cm^{-2}. **b)** Capacity-limited cycling of a Cu/LPSC/NMC full cell with a cathode loading of 3 mAh cm^{-2} and a current density of 0.5 mA cm^{-2}. Each half cycle was controlled to cycle 1 mAh cm^{-2} of capacity after the initial charge. **c)** Limited cycling of a Cu/LPSC/Li half cell at 0.5 mA cm^{-2} with an initial deposition step of 1 mAh cm^{-2} and subsequent half cycles of 0.5 mAh cm^{-2}. **d)** Limited cycling of a Cu/LPSC/Li half cell at 0.5 mA cm^{-2} with an initial deposition step of 3 mAh cm^{-2} and subsequent half cycles of 2.3 mAh cm^{-2}.

An important observation from these limited capacity experiments is that the amount of lithium remaining at the interface strongly impacts cell stability and short circuiting. Figure 6c shows that a cell that cycled 50% of a lower initial capacity of 1 mAh cm^{-2} short circuited after plating a cumulative capacity of only ~25 mAh cm^{-2} onto Cu, which was much lower than the cell in Fig. 6a that had higher initial capacity. Polarization eventually occurred during stripping (see the 45th cycle in Fig. 6c), which was likely associated with local lithium depletion and was accompanied by the return of the nucleation overpotential. The reduced lifetime of this cell compared to Fig. 6a can be attributed to the thinner amount of lithium left at the interface after stripping (~2.5 μm, 0.5 mAh cm^{-2}), which was less effective in preventing complete removal of lithium from certain regions of the interface. Similar behavior was observed with a cell that had a thicker initial layer of 3 mAh cm^{-2} but cycled 75% of the capacity instead of 50% (Fig. 6d). Although the initial cycles exhibited stable voltages, the cell began to polarize during the 8th stripping step (green curve), followed by re-nucleation and ultimately short circuiting in the 10th cycle. Like the cell in Fig. 6c, less lithium was left at the interface after stripping (~3.75 μm, 0.75 mAh cm^{-2}), making it more likely that some regions would be stripped of lithium entirely and lose active area. These results emphasize the importance of retaining electrochemically active area during stripping at anode-free interfaces.

Strategic electrochemical protocols to carefully control interfacial characteristics, such as those shown in Fig. 6, will likely play an important role in the development of anode-free SSBs. While we have shown the benefits of retaining lithium at the interface by controlling cycle capacity after initial lithium deposition, the protocols demonstrated in Fig. 6 are not feasible for commercial batteries because they reduce specific energy and energy density. The cathode loading utilization must be maximized to achieve a high reversible areal capacity and avoid the energy penalty of unused heavy cathode particles. For example, an anode-free cell with a cathode loading of 5 mAh cm^{-2} and 100% capacity utilization would have a stack-level energy density of ~1500 Wh L^{-1} in the discharged state. Decreasing the utilization to 50%, as presented in this work, would reduce the energy density to ~750 W L^{-1}, which is only on par with the stack-level energy density of conventional lithium-ion batteries using graphite anodes[38]. Although the protocols in this work are not viable for high-energy SSBs, we envision that careful optimization of electrochemical protocols during the end of discharge and at the beginning of charge will be needed to stabilize anode-free cycling while minimizing energy density penalties.

3. Conclusions

This work has demonstrated the feasibility of plating and stripping lithium metal in sulfide-based anode-free SSBs, and through this effort we have revealed degradation mechanisms unique to anode-free SSBs. Using the sulfide SSE Li_6PS_5Cl, anode-free cells were assembled via simple uniaxial cold pressing at ~15 MPa. Large quantities of lithium (> 5 mAh cm^{-2}) could be plated at room temperature onto the current collector at a relatively high current density of 1 mA cm^{-2} without short circuiting. However, lithium plating and stripping was found to be nonuniform across the interface, causing local depletion of lithium in some regions and decreasing the electrochemically active area. Current constriction effects created by the loss of active area likely increased the stripping current density beyond a critical value to form voids at these remaining lithium regions. These voided lithium regions are highly susceptible to filament nucleation during subsequent plating steps due to current constriction near the voids. This mechanism is different than that found in lithium-excess SSBs and is expected to be general for any anode-free SSE chemistry. Despite this key limitation, it was shown that anode-free full cells exhibited comparable Coulombic efficiencies to full cells with thick lithium metal foils. In contrast to conventional wisdom, then, it is short circuiting which is the key limitation of anode-free SSBs rather than the minimal lithium inventory. Finally, it was shown that retaining thin lithium at the interface could mitigate local lithium depletion and greatly improve cycling behavior.

Our new findings herein provide important guidance for the engineering of anode interfaces for enabling high-performance anode-free SSBs. While relatively thick (~10 μm) Ag-C layers have demonstrated improved cyclability at SSB anode interfaces[13], it would be beneficial to develop solutions that occupy minimal volume and mass to maximize energy density/specific energy. Our results illustrate the importance of mitigating local lithium depletion and the loss of electrochemically active area when fully stripping lithium. Without modifying the interface, it may be unavoidable to form isolated lithium regions at the end of stripping, but careful control of stripping currents and/or voltages could be beneficial for preventing local voiding at these regions. Other solutions that could be effective include interfacial layers that homogenize electrochemical reactions and/or transport at the interface. For instance, interfacial layers that enable Li transport via diffusion to compensate for local lithium depletion could be effective for mitigating current constriction and void formation.

Methods

Materials

Li_6PS_5Cl powder (NEI Corporation) was prepared for use as the SSE separator by hand grinding ~600 mg in a mortar and pestle for ~20 min to reduce the particle size. Copper foil with a thickness of ~10 μm (MTI) was used as the deposition substrate in anode-free cells. Lithium metal foil (99.9% purity, MSE Supplies) was cleaned before use by rubbing off the surface contamination layer. Composite cathodes were fabricated using a 70:27.5:2.5 weight ratio of single crystal $LiNi_{0.6}Mn_{0.2}Co_{0.2}O_2$ (NMC, MSE Supplies), ultrafine LPSC (MSE Supplies, particle size < 1 μm), and vapor-grown carbon fibers (Sigma Aldrich). To reduce side reactions with LPSC, NMC particles were coated with $LiNb_{0.5}Ta_{0.5}O_3$ (LNTO) following a previously reported procedure[39,40]. The powders were milled together in a planetary ball mill (Fritsch Pulverisette 7) using a zirconia jar with eight 10 mm zirconia balls and ~1 g of composite. A protocol of 10 min of milling at 150 RPM followed by 5 min of rest was applied for 3 cycles to yield the mixed composite cathode.

Assembly and testing of solid-state batteries

SSBs in this study used custom cell housings that were calibrated to apply known amounts of stack pressure by controlling the torque applied to the cell bolts, as based on previous studies[21,40,41]. Anode-free half cells were assembled in an Ar-filled glovebox by first loading 90 mg of ground LPSC into a 10 mm PEEK die and cold pressing in a uniaxial press at 375 MPa for 1 min to form a dense pellet. 10-mm-diameter copper discs were punched out and subsequently cleaned by sonicating in acetone and IPA, followed by blow drying with nitrogen gas. A copper disc was then pressed onto one side of the LPSC pellet using a titanium rod. Lithium metal foil was incorporated by pressing a disc with a thickness of ~0.3 mm onto another titanium rod, cleaning the pressed foil with a toothbrush, and inserting the rod into the die. The entire cell stack was then uniaxially compressed at 15 MPa for 5 min to establish contact at the electrode/SSE interfaces. The cell was then placed between two steel plates and compressed at the desired stack pressure for operation (typically 15 MPa).

Anode-free full cells used a slightly modified assembly procedure. 90 mg of ground LPSC was loaded into the die and compressed by hand to form a compact layer. Composite cathode powder was then poured on top and compressed by hand to form the cathode layer. The areal capacity loading varied between cells as specified in the text, with 1 mAh cm^{-2} being equivalent to 5.9 mg of composite (assuming a specific capacity of 190 mAh g^{-1}). The cell stack was then

cold-pressed uniaxially at 375 MPa for 1 min to densify the layers. Afterwards, a cleaned copper disc was inserted on the anode side of the LPSC layer. The cell was then placed between plates and compressed to a stack pressure of 15 MPa. For full cells using a thick lithium foil instead of an anode-free substrate, lithium metal was incorporated using the same procedure as the anode-free half cells.

Electrochemical experiments were conducted inside an Ar-filled glove box to prevent air exposure. SSBs were tested using a Landt battery cycler or BioLogic SP-200 potentiostat. Electrochemical impedance spectroscopy (EIS) was performed using a frequency range of 2 MHz to 2 Hz and a voltage amplitude of 10 mV.

Characterization

Cryogenic focused ion beam (cryo-FIB) experiments were conducted using a Thermo Fisher Helios 5CX FIB-SEM equipped with a Ga ion source and Quorum cryogenic stage system. Samples were extracted from cells and taken for characterization during the same day. The samples were rapidly transferred into the vacuum chamber, with an air exposure time of ~30 s. We found that the lithium metal layer was not oxidized due to it being confined between the LPSC and copper layers. Before milling, samples were cooled to -145 °C to reduce detrimental interactions with the ion beam. No protective layers were deposited before milling due to the presence of the copper foil. Initial milling cuts were performed using an ion accelerating voltage of 30 kV and beam current of 45 nA. Final cuts were made at 30 kV and 2.8 nA. Images were collected using an Everhart-Thornley secondary electron detector with an accelerating voltage of 5 kV and current of 0.34 nA.

X-ray tomography scans of anode-free SSBs were collected at the Advanced Photon Source's 2-BM beamline using monochromatic X-rays with an energy of 25.5 keV. 1500 projections were collected over 180° with an exposure time of 400 ms using an optics system consisting of an Oryx 5.0 MP Mono 10GigE detector and a 2× magnification lens. The field of view was ~4.2 by 1.7 mm^2 and the voxel size was 1.7 μm. The anode-free SSB for X-ray tomography was assembled using a specialized cell housing that was smaller than the other housings used herein[14]. This design was chosen to reduce X-ray absorption while maintaining an airtight seal and applying stack pressure. 7 mg of ground LPSC was inserted into the housing and compressed at 225 MPa. A 2 mm disc of Grafoil was placed on one side of the LPSC layer, followed by a 2 mm disc of lithium metal on the other side. Grafoil was chosen as the deposition substrate due to the strong X-ray absorption of metals like copper and stainless steel, which diminishes the ability

to resolve lithium metal at the interface. Screws were inserted on each side of the cell and tightened to a torque of 0.1 N-m (corresponding to a stack pressure of ~10 MPa). A MACCOR 4300 battery cycler was used to deposit lithium metal at a current density of 0.5 mA cm^{-2}. TomoPy was used to reconstruct the raw data into images via the GridRec method. Fiji's Trainable Weka Image Segmentation plugin was used to segment the deposited lithium metal in the reconstructed images. The segmented images were then processed in MATLAB to analyze thickness variation across the interface.

Images of the deposited lithium cross-section were collected using both optical microscopy and scanning electron microscopy (SEM). Samples were prepared by depositing lithium metal at 0.5 mA cm^{-2}, extracting from the PEEK die, and cutting the cross-section with a scalpel. This preparation method was observed to introduce some imaging defects, such as vertical streaks in the lithium metal and contamination particles from the SSE (see Fig. 1). Optical images were collected using a Keyence VHX-600 digital microscope. SEM images were taken using a Zeiss Ultra 60 SEM with an accelerating voltage of 10 kV.

X-ray photoelectron spectroscopy (XPS) measurements were conducted using a Thermo K-Alpha XPS instrument. The sample was prepared by depositing lithium onto copper at 0.5 mA cm^{-2} in an anode-free half cell for 56 hours. The cell was then disassembled and the lithium layer was removed from the electrolyte and copper foil using a razor. The sample was transferred into the XPS instrument without exposure to ambient air using a vacuum sealed transfer holder. The sample was irradiated with an X-ray beam from an Al Kα source using a 400 μm spot size. The base pressure in the XPS chamber was less than 2.5×10^{-7} mbar and the surface charging effect was compensated with a flood gun with slow electrons and Ar+ ions. To minimize the signal from surface contaminants, each spectrum was collected after etching the sample surface with the ion beam for 1140 seconds.

Acknowledgments

J.A.L. acknowledges support from a NASA Space Technology Research Fellowship. S.E.S. acknowledges support from an NSF Graduate Research Fellowship under Grant No. DGE-1650044 and a Sloan Foundation MPHD Program Scholarship. This work was performed in part at the Georgia Tech Institute for Electronics and Nanotechnology, a member of the National Nanotechnology Coordinated Infrastructure (NNCI), which is supported by the National Science Foundation (ECCS-2025462). Support is acknowledged from NASA Grant Number

80NSSC21M0101. This research used resources of the Advanced Photon Source, a U.S. Department of Energy (DOE) Office of Science user facility operated for the DOE Office of Science by Argonne National Laboratory under Contract No. DE-AC02-06CH11357.

Author Contributions

J.A.L. and M.T.M. conceived the study. J.A.L. built the solid-state batteries and tested them. J.A.L. and S.E.S. conducted the cryogenic FIB experiments. Y.L. synthesized and prepared materials for cathodes. J.A.L., S.E.S., and D.L.N. collected the X-ray tomography data. S.G.Y. performed the XPS experiments and analysis. P.S. assisted with the use of beamline 2-BM and reconstruction processing. J.A.L. analyzed the data and wrote the manuscript with M.T.M.

References

1. Janek, J. & Zeier, W. G. A solid future for battery development. *Nat. Energy* **1**, 16141 (2016).
2. Shen, Y. *et al.* Unlocking the energy capabilities of lithium metal electrode with solid-state electrolytes. *Joule* **2**, 1674–1689 (2018).
3. Hatzell, K. B. *et al.* Challenges in lithium metal anodes for solid- state batteries. *ACS Energy Lett.* **5**, 922-934 (2020).
4. Albertus, P., Babinec, S., Litzelman, S. & Newman, A. Status and challenges in enabling the lithium metal electrode for high-energy and low-cost rechargeable batteries. *Nat. Energy* **3**, 16–21 (2018).
5. Famprikis, T., Canepa, P., Dawson, J. A., Islam, M. S. & Masquelier, C. Fundamentals of inorganic solid state electrolytes for batteries. *Nat. Mater.* **18**, 1278-1291 (2019).
6. Nanda, S., Gupta, A. & Manthiram, A. Anode-free full cells: A pathway to high-energy density lithium-metal batteries. *Adv. Energy Mater.* **11**, 2000804 (2021).
7. Heubner, C. *et al.* From lithium-metal toward anode-free solid-state batteries: Current developments, issues, and challenges. *Adv. Funct. Mater.* **31**, 2106608 (2021).
8. Louli, A. J. *et al.* Diagnosing and correcting anode-free cell failure via electrolyte and morphological analysis. *Nat. Energy* **5**, 693–702 (2020).
9. Qian, J. *et al.* Anode-free rechargeable lithium metal batteries. *Adv. Funct. Mater.* **26**, 7094–7102 (2016).
10. Weber, R. *et al.* Long cycle life and dendrite-free lithium morphology in anode-free lithium pouch cells enabled by a dual-salt liquid electrolyte. *Nat. Energy* **4**, 683–689 (2019).
11. Salvatierra, R. V., Chen, W. & Tour, J. M. What can be expected from “anode-free” lithium metal batteries? *Adv. Energy Sustain. Res.* **2**, 2000110 (2021).

12. Wang, M. J., Carmona, E., Gupta, A., Albertus, P. & Sakamoto, J. Enabling “lithium-free” manufacturing of pure lithium metal solid-state batteries through in situ plating. *Nat. Comm.* **11**, 5201 (2020).

13. Lee, Y. G. *et al.* High-energy long-cycling all-solid-state lithium metal batteries enabled by silver–carbon composite anodes. *Nat. Energy* **5**, 299–308 (2020).

14. Lewis, J. A. *et al.* Linking void and interphase evolution to electrochemistry in solid-state batteries using operando X-ray tomography. *Nat. Mater.* **20**, 503–510 (2021).

15. Kasemchainan, J. *et al.* Critical stripping current leads to dendrite formation on plating in lithium anode solid electrolyte cells. *Nat. Mater.* **18**, 1105-1111 (2019).

16. Wang, M. J., Choudhury, R. & Sakamoto, J. Characterizing the Li-solid-electrolyte interface dynamics as a function of stack pressure and current density. *Joule* **3**, 2165-2178 (2019).

17. Krauskopf, T., Hartmann, H., Zeier, W. G. & Janek, J. Toward a fundamental understanding of the lithium metal anode in solid-state batteries - An electrochemo-mechanical study on the garnet-type solid electrolyte $Li_{6.25}Al_{0.25}La_3Zr_2O_{12}$. *ACS Appl. Mater. Interfaces* **11**, 14463–14477 (2019).

18. Cheng, E. J., Sharafi, A. & Sakamoto, J. Intergranular Li metal propagation through polycrystalline $Li_{6.25}Al_{0.25}La_3Zr_2O_{12}$ ceramic electrolyte. *Electrochim. Acta* **223**, 85–91 (2017).

19. Porz, L. *et al.* Mechanism of lithium metal penetration through inorganic solid electrolytes. *Adv. Energy Mater.* **7**, 1701003 (2017).

20. Kazyak, E. *et al.* Li penetration in ceramic solid electrolytes: operando microscopy analysis of morphology, propagation, and reversibility. *Matter* **2**, 1025-1048 (2020).

21. Lewis, J. A. *et al.* Role of areal capacity in determining short circuiting of sulfide-based solid-state batteries. *ACS Appl. Mater. Interfaces* **14**, 4051–4060 (2022).

22. Ning, Z. *et al.* Visualizing plating-induced cracking in lithium-anode solid-electrolyte cells. *Nat. Mater.* **20**, 1121-1129 (2021).

23. Hobold, G. M. *et al.* Moving beyond 99.9% Coulombic efficiency for lithium anodes in liquid electrolytes. *Nat. Energy* **6**, 951–960 (2021).

24. Xiao, J. *et al.* Understanding and applying coulombic efficiency in lithium metal batteries. *Nat. Energy* **5**, 561–568 (2020).

25. Fan, X. *et al.* Fluorinated solid electrolyte interphase enables highly reversible solid-state Li metal battery. *Sci. Adv.* **4**, eaau924 (2018).

26. Ji, X. *et al.* Solid-state electrolyte design for lithium dendrite suppression. *Adv. Mater.* **32**, 2002741 (2020).

27. Lee, M. J. *et al.* Elastomeric electrolytes for high-energy solid-state lithium batteries. *Nature* **601**, 217–222 (2022).

28. Krauskopf, T. *et al.* Lithium metal growth kinetics on LLZO garnet type solid electrolytes – *operando* study of lithium deposition and dendrite growth. *Joule* **3**, 2030-2049 (2019).

29. Davis, A. L., Kazyak, E., Liao, D. W., Wood, K. N. & Dasgupta, N. P. Operando analysis of interphase dynamics in anode-free solid-state batteries with sulfide electrolytes. *J. Electrochem. Soc.* **168**, 070557 (2021).

30. Motoyama, M., Ejiri, M. & Iriyama, Y. Modeling the nucleation and growth of Li at metal current collector/LiPON interfaces. *J. Electrochem. Soc.* **162**, A7067 (2015).

31. Cortes, F. J. Q., Lewis, J. A., Tippens, J., Marchese, T. S. & McDowell, M. T. How metallic protection layers extend the lifetime of NASICON-based solid-state lithium batteries. *J. Electrochem. Soc.* **167**, 050502 (2020).

32. Kim, S. *et al.* The role of interlayer chemistry in Li-metal growth through a garnet-type solid electrolyte. *Adv. Energy Mater.* **10**, 1903993 (2020).

33. Doux, J. M. *et al.* Stack pressure considerations for room-temperature all-solid-state lithium metal batteries. *Adv. Energy Mater.* **10**, 1903253 (2020).

34. Wood, K. N. & Teeter, G. XPS on Li-battery-related compounds: Analysis of inorganic SEI phases and a methodology for charge correction. *ACS Appl. Energy Mater.* **1**, 4493-4504 (2018).

35. Wenzel, S., Sedlmaier, S. J., Dietrich, C., Zeier, W. G., Janek, J. Interfacial reactivity and interphase growth of argyrodite solid electrolytes at lithium metal electrodes. *Solid State Ion.* **318**, 102-112 (2018).

36. Athanasiou, C. E. *et al.* Rate-dependent deformation of amorphous sulfide glass electrolytes for solid-state batteries. *Cell Rep. Phys. Sci.* **3**, 100845 (2022).

37. Papakyriakou, M. *et al.* Mechanical behavior of inorganic lithium-conducting solid electrolytes. *J. Power Sources* **516**, 230672 (2021).

38. Lewis, J. A., Cavallaro, K. A., Liu, Y. & McDowell, M. T. The Promise of Alloy Anodes for Solid-State Batteries. *Joule* (In press).

39. Zhang, W. *et al.* Interfacial processes and influence of composite cathode microstructure controlling the performance of all-solid-state lithium batteries. *ACS Appl. Mater. Interfaces* **9**, 17835–17845 (2017).

40. Han, S. Y. *et al.* Stress evolution during cycling of alloy-anode solid-state batteries of alloy-anode solid-state batteries. *Joule* **5**, 2450-2465 (2021).

41. Lee, C. *et al.* Stack pressure measurements to probe the evolution of the lithium-solid-state electrolyte interface. *ACS Energy Lett.* **6**, 3261–3269 (2021).